(Received 29 December 2023, Accepted 9 March 2024, Scheduled 18 March 2024)

Optimization of Electromagnetic Thrust for Short Primary Unilateral Linear Induction Motor

Cheng Wen*, Junyi Chen, Jian Cui, Zhiping Wan, and Yujian Chang

Hebei Provincial Collaborative Innovation Center of Transportation Power Grid Intelligent Integration Technology and Equipment
School of Electrical and Electronic Engineering, Shijiazhuang Tiedao University, Hebei 050043, China

ABSTRACT: In this paper, four different structures are proposed to optimize electromagnetic thrust for the primary and secondary pole linear induction motors. Firstly, the two-dimensional topology structure of the motor is established, and the correlation equation of electromagnetic thrust is established. Secondly, the electromagnetic thrust optimization of the primary structure of the motor is carried out by the chamfer method and trapezoidal structure method. Then, the secondary structure of the motor is slotted and mixed with different conductivity materials to optimize the electromagnetic thrust. At the same time, a motor model with high permeability under ideal conditions is proposed from the angle of relative permeability of secondary aluminum plate. Finally, the four optimized structures were simulated, and the changes of electromagnetic thrust, air gap density, and back electromotive force were analyzed. The simulation results fully verify the effectiveness of the four optimization structures proposed in this paper.

1. INTRODUCTION

With the development of domestic economy, the rapid expansion and development of core cities in various regions, it is extremely important to strengthen regional interconnection, which also means that new requirements are put forward for China's urban rail transit [1].

The operation mode of short primary single-side linear induction motor in urban rail transit system is divided into two types: linear wheel-rail transit and maglev transit [2]. The former has lower requirements for construction conditions, such as strong climbing and turning performance, flexible line planning, and low construction costs. The latter leads in speed and comfort [3–5]. Intersecting the traditional mode of transportation, the linear motor traction system is not limited to the adhesion traction between the wheel and rail [6], so it can greatly pursue speed improvement, and combined with power electronics technology and computer control technology, linear induction motor will be widely used in the future [7, 8].

In the rail transit system, the primary and secondary linear induction motors are respectively installed in the train and the running track. When a symmetrical three-phase alternating current is passed into the primary winding, the train moves in a straight line through the traction of the electromagnetic thrust inside the motor [9]. Due to the primary and secondary disconnection of the linear motor, the magnetic field will produce non-uniformity when the motor enters the end, resulting in uneven current density and uneven force, so there will be end effects and normal forces, and in order to avoid the collision of the primary and secondary [10], the air gap of the linear motor must be large enough to cause the power factor and energy transfer efficiency of the motor to be reduced [11].

In this paper, the structure of the short primary single-side linear induction motor was optimized, and Maxwell 2D finite element analysis was adopted [12–14]. Firstly, the primary structure of the motor was optimized, and the thrust was improved by chamfering method and adding a trapezoidal structure at the end [15]. Secondly, the secondary structure of the motor was optimized, and the thrust was optimized by cap and slot method on the secondary plate [16, 17]. Finally, materials with different relative permeabilities are set to test the electromagnetic thrust of the motor, and it is inferred that the electromagnetic thrust of the linear motor will increase with the increase of the relative permeability.

2. MODEL DEVELOPMENT AND PARAMETER SETTING

2.1. Linear Induction Motor in Urban Rail Transit

In the vast majority of urban rail transit systems, linear induction motor traction technology is adopted. Fig. 2 shows the principle structure diagram of the motor, and the linear induction motor primary and secondary are installed on the train bo-

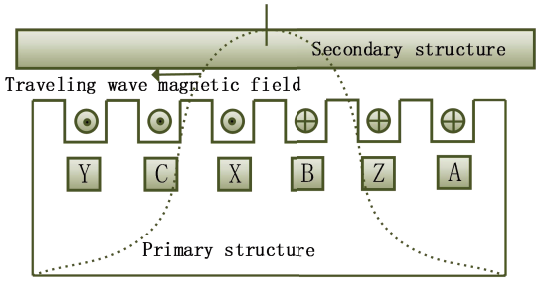

FIGURE 1. Schematic diagram of linear induction motor.

* Corresponding author: Cheng Wen (wencheng0308@163.com).

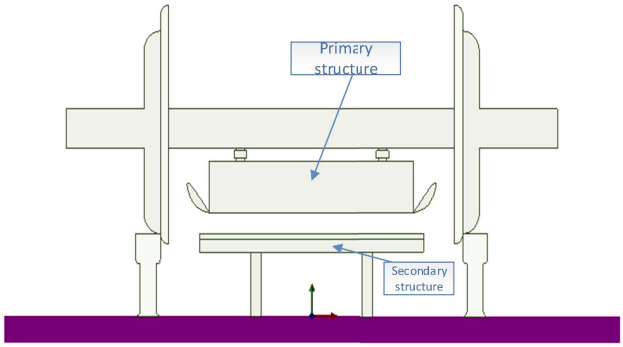

FIGURE 2. Linear induction motor structure diagram.

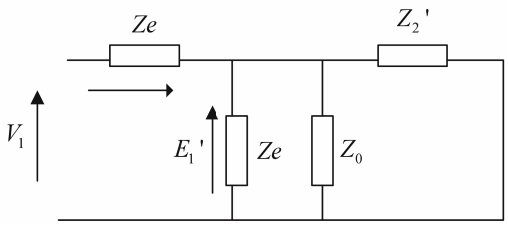

FIGURE 3. Linear induction motor equivalent circuit.

gie and running track. The primary is composed of iron core and winding, and the secondary is composed of magnetic permeability and conductive layer. When the primary winding of the linear induction motor is fed into the three-phase AC, the air gap between the primary and secondary will produce a traveling wave magnetic field. As shown in Fig. 1, under the cutting of the traveling wave magnetic field, the secondary will induce the electromotive force and generate the induced current. When the induced current interacts with the magnetic field in the air gap, the electromagnetic thrust will be generated. The motor will move forward or backward according to the fixed ways of the primary and secondary.

2.2. Two-Dimensional Modeling Analysis of Linear Induction Motor

The expression of electromagnetic thrust, efficiency, and power factor combined with linear induction motor is as follows [4, 5]:

$$F_x = \frac{m_1}{v_s} \cdot \frac{(1-k_e)^2 E_1^2}{|Z_2'|} \cdot \frac{R_2'(s)}{s} - \Delta F_m \tag{1}$$

$$\eta = \frac{1}{P_m}\left[m_1(1-k_e)^2 \frac{E_1^2}{|Z_2'|} \cdot \frac{R_2'(s)}{s}(1-s) - \Delta P_m\right] \tag{2}$$

$$\cos\varphi = \frac{\mathrm{Re}\left[Z_1 + Z_t\left(1-k_e\right)\right]}{\left|Z_1 + Z_t\left(1-k_e\right)\right|} \tag{3}$$

Among them,

m_1: the number of phases of the primary winding;
v_s: synchronization speed;
k_e: longitudinal end effect coefficient;
Z_2': secondary impedance converted to the primary side;
E_1: The induced electromotive force of the primary winding ignoring the longitudinal end effect;
ΔF_m: Thrust corresponding to mechanical losses;
P_m: Input power of the power supply.

According to the original data of the motor, the main size of the motor can be designed according to the following:

(1) Polar distance

$$\tau = v_s/(2f) = 70\,\mathrm{mm} \tag{4}$$

(2) Number of poles

$$2p = 7 \tag{5}$$

(3) Longitudinal length of primary core

$$L = 2p\tau = 490\,\mathrm{mm} \tag{6}$$

(4) The normal height of the primary core must meet the strength requirements of mechanical installation

$$h_t = 50\,\mathrm{mm} \tag{7}$$

(5) Thickness of primary core lamination (primary transverse width)

$$l_c = \frac{0.25P_\delta}{aw0.707B_{3y}\left(AS\right)fp\tau^2 k_{w1}} = 84\,\mathrm{mm} \tag{8}$$

(6) secondary transverse width

In general, when the secondary width of the board is reached in relation to the primary width

$$l_s = l_c + \frac{\lambda}{\pi} \tag{9}$$

When the ratio of thrust to size of primary and secondary meets the following formula,

$$l_s = l_c + \frac{\lambda}{\pi} = 128\,\mathrm{mm} \tag{10}$$

According to the above calculation data in Figure 3, the main size parameters of the linear induction motor can be determined, but because there is an electromagnetic air gap between the secondary aluminum plates of the composite secondary mechanical air gap of the linear induction motor, and the size of the electromagnetic air gap is related to the performance of the motor, the thrust and other parameters of the motor are directly affected. The larger the electromagnetic air gap of the motor is, the larger the magnetoresistance of the motor is, and the smaller the excitation reactance is. The thinner the secondary aluminum plate is, the larger the secondary resistance of the motor is, the smaller the eddy current is, and the smaller the thrust is, so it is necessary to determine the size of the electromagnetic air gap of the secondary aluminum plate as accurately

Primary length: 486 mm	Number of slots: 41
Primary altitude: 50 mm	Polar distance: 70 mm
Primary slot width: 6.8 mm	Al conductivity: $3.8 * 10^7$
Primary groove depth: 35 mm	Electrical conductivity of Fe: $1.03 * 10^7$
Pitch of teeth: 11.7 mm	voltage: 220 V
Secondary width: 128 mm	frequency: 50 Hz
Secondary Al thickness: 4 mm	Number of turns: 68
Secondary Fe thickness: 8 mm	Mechanical air gap: 4 mm

TABLE 1. Motor model data.

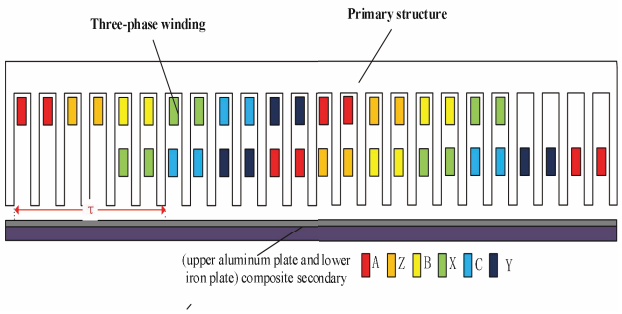

FIGURE 4. Motor topology model diagram.

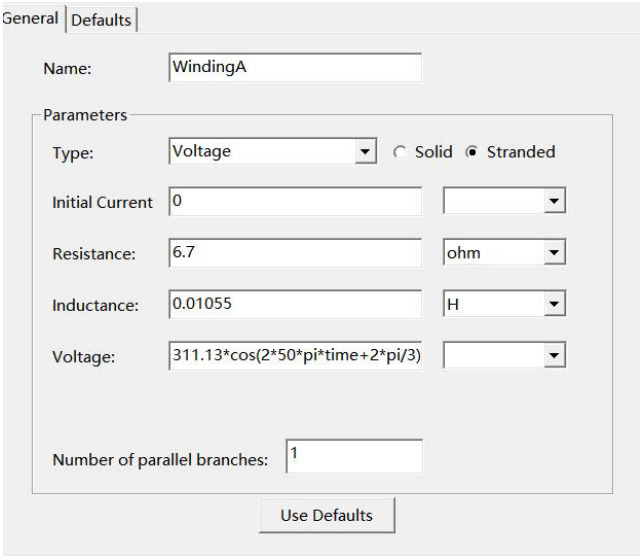

FIGURE 5. Maxwell indicates the two-dimensional data adjustment diagram.

FIGURE 6. Chamferstructure finite element diagram.

Chamfer Angle	Chamfer height/mm	Chamfer bottom edge/mm	The tangent of the chamfer
0°	0	23.34	0
12.29°	5	23.34	0.2178
19.63°	8	23.34	0.3566
36.80°	17.5	23.34	0.7480

TABLE 2. Chamfer data.

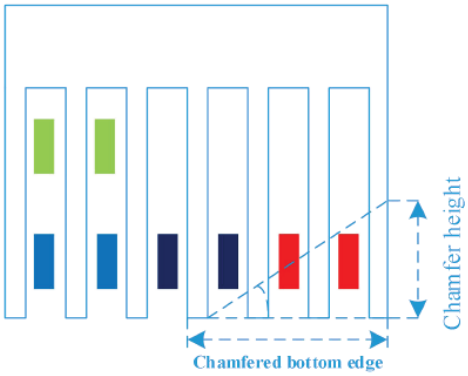

FIGURE 7. Chamfer structure diagram.

as possible. The motor parameters used in this experiment are shown in Table 1, and the specific setting conditions of the finite element are shown in Figures 4 and 5.

2.3. Optimal Design of Primary Structure

(Method 1) the chamfering method: by chamfering the primary end of the linear induction motor, the chamfering method can improve the stability and efficiency of the motor:

1. Reduce electromagnetic field fluctuations to make it run more smoothly;

2. Reduce the electromagnetic damping of the primary end to make it move faster and improve efficiency.

Because the outlet end of linear induction motor will enhance the eddy current effect during operation, a certain chamfering is set at the outlet end to reduce the influence of the end effect. Chamfer data is shown in Table 2. By setting different angles

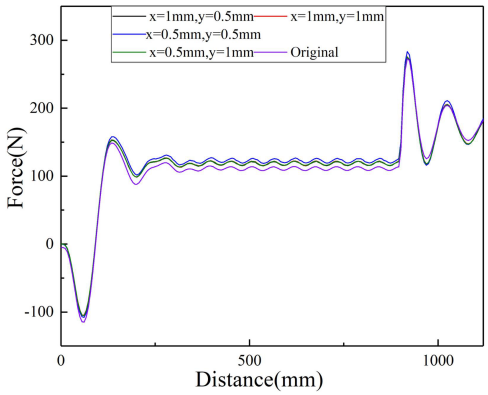

FIGURE 8. Electromagnetic thrust comparison diagram.

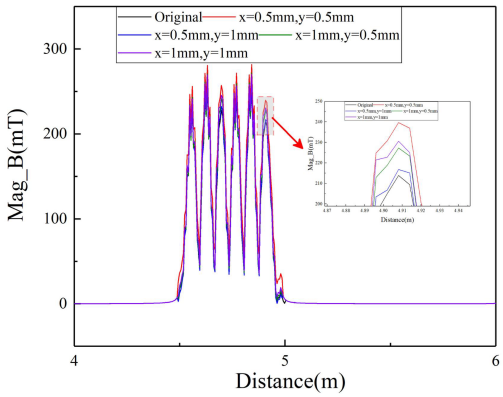

FIGURE 9. Back electromotive force comparison diagram (phase A for example).

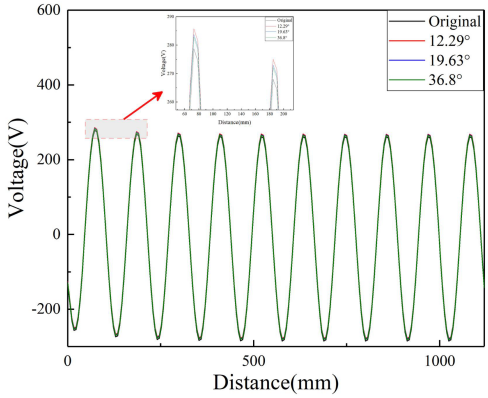

FIGURE 10. Magnetic density comparison diagram of air gap.

FIGURE 11. Trapezoidal structure finite element diagram.

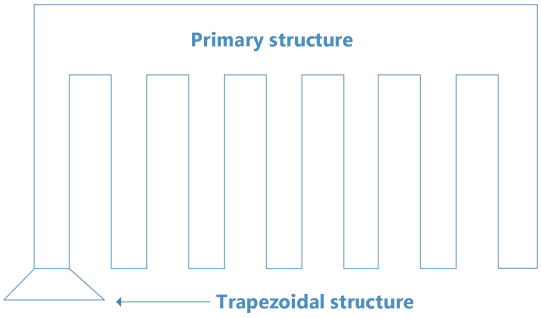

FIGURE 12. Primary bottom trapezoidal structure diagram.

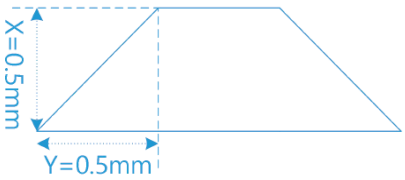

FIGURE 13. Trapezoidal structure 1.

to observe the thrust increase degree, the chamfering method can increase the thrust to a certain extent.

In Figs. 6–10, compared to the electromagnetic thrust of the initial motor, it is found that adding a chamfer structure to the primary end of the motor can increase the thrust to a certain extent. Since the angle of the primary outlet cannot be too large, the angle of the chamfer is controlled at 0–45° as far as possible in the experiment. With the continuous change of the chamfer angle, the thrust will be larger than the electromagnetic thrust of the initial structure. At the same time, the magnetic density of the air gap is positively correlated with the thrust, so the results of the magnetic density of the air gap are also compared and analyzed from four angles in the experiment. It is confirmed by the data that setting a certain angle at the outlet of the linear induction motor can improve the thrust of the linear induction motor, so it can be used as a method for the subsequent research on the thrust of the linear induction motor.

(Method 2) Primary end with trapezoidal structure:

The trapezoidal structure of different structures is added to the bottom of the primary structure, and different trapezoidal structures are set according to different bottom edges and heights. The structure is as shown in Figs. 11–16.

Because changes in the primary structure can affect the electromagnetic thrust, four different trapezoidal structures are used at the end of the primary to test the electromagnetic performance of the motor, and then the thrust, air gap magnetic den-

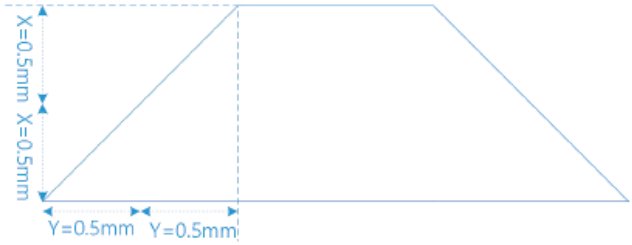

FIGURE 14. Trapezoidal structure 2.

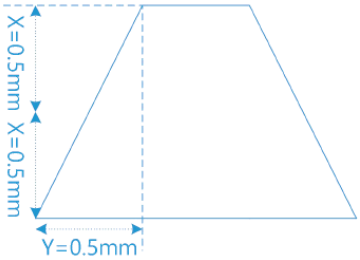

FIGURE 15. Trapezoidal structure 3.

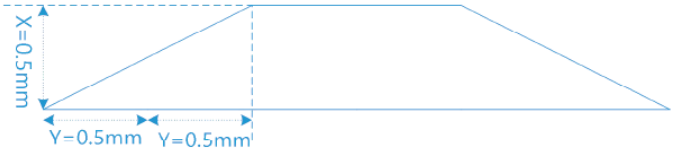

FIGURE 16. Trapezoidal structure 4.

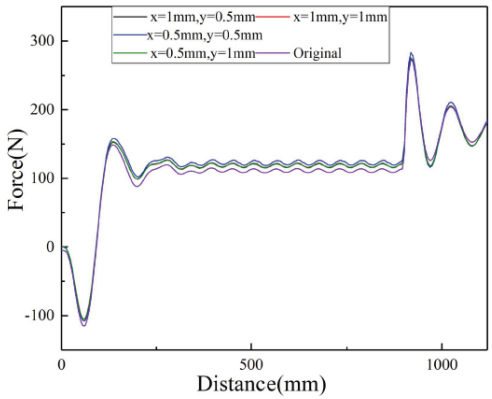

FIGURE 17. Comparison of electromagnetic thrust of four trapezoidal structures.

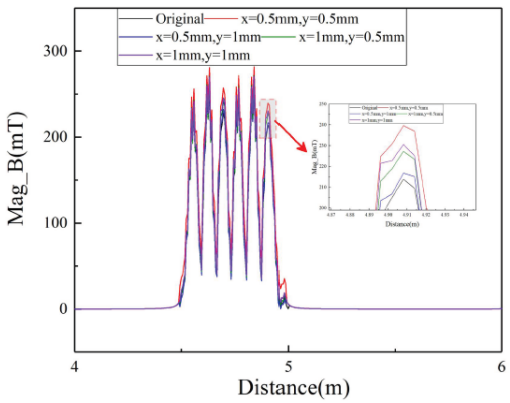

FIGURE 18. Comparison of air-gap magnetic density of four trapezoidal structures.

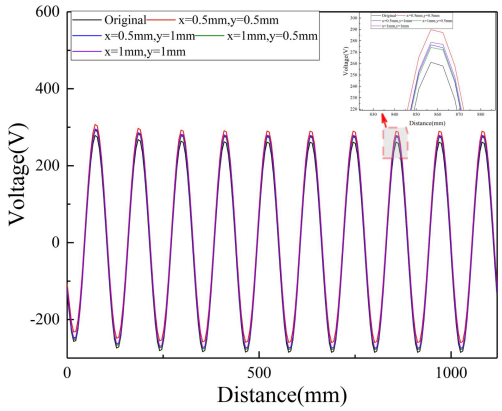

FIGURE 19. Comparison diagram of back electromotive forces of four trapezoidal structures (phase A as an example).

sity, and back electromotive force are simulated and tested without changing other conditions.

After the initial simulation experiment with different trapezoidal structures in Fig. 17–19, it is found that when the linear induction motor is initially added with a trapezoidal structure of $X = 0.5\,\text{mm}/Y = 0.5\,\text{mm}$, the thrust and air-gap magnetic density are larger than that of other structures. The thrust increases by about 15 N, and the air-gap magnetic density increases by 0.3 Tesla. The back electromotive force is increased by about 15 V, and compared with other structures, this structure is simpler, and the added structure cost is lower. Due to the structural characteristics of the linear induction motor itself — the primary and secondary structures are disconnected, so the trapezoidal structure added at the bottom of the primary should not be too large, thus the bottom edge and height are the most appropriate 0.5 mm.

2.4. Secondary Structure Optimization

(Structure 1) The secondary plate is slotted (This method is derived from the three-dimensional structure model of linear induction motor).

Conventional structure is the complete structure: simple structure, low cost but large lateral force. As shown in Fig. 20, secondary plate slot structure, composed of an aluminum slit and background iron plate, can reduce eddy current. Beyond the three-dimensional structure, the secondary plate is slotted

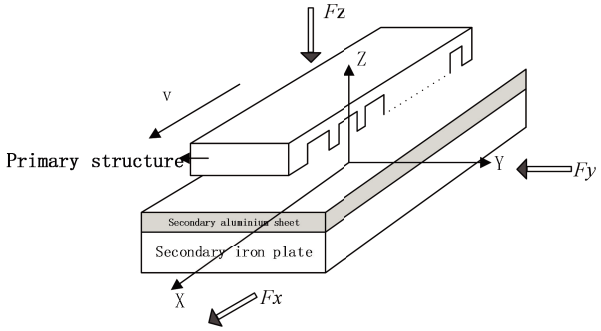

FIGURE 20. Motor 3D structure diagram.

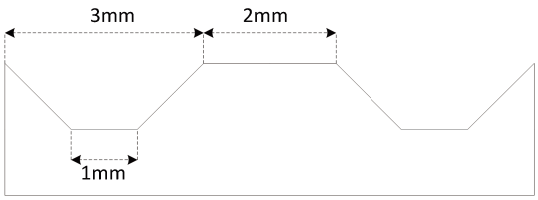

FIGURE 21. Spacing 2 mm.

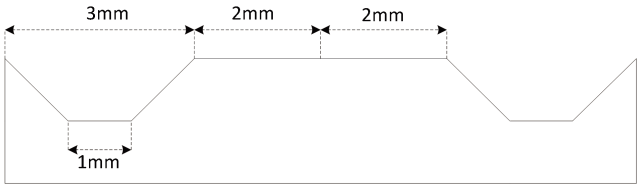

FIGURE 22. Spacing 4 mm.

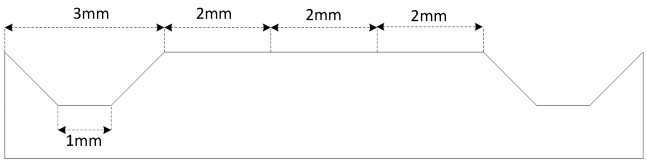

FIGURE 23. Spacing 6 mm.

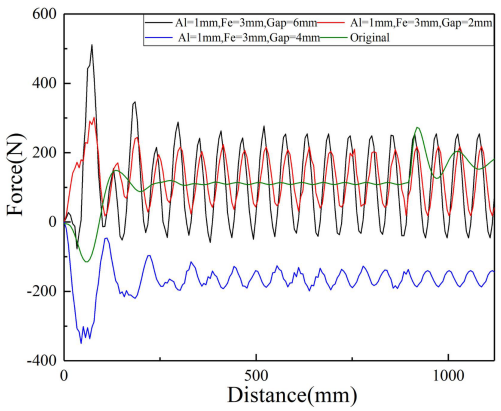

FIGURE 24. Comparison of electromagnetic thrust of three spacer structures.

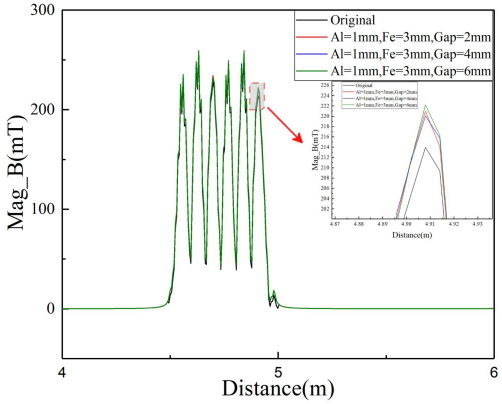

FIGURE 25. Comparison of air-gap magnetic density of three spacer structures.

in two dimensions, and the trapezoidal structure is also adopted throughout the transverse surface of the aluminum plate. By opening different trapezoidal slots on the secondary aluminum plate, different trapezoidal slot spacing structures are given.

As shown in Figs. 21–23, after the secondary aluminum plate is slotted and treated with different intervals: the simulation experiment with intervals of 2 mm, 4 mm, and 6 mm, the thrust, air gap magnetic density, and anti-reaction electromotive force are observed.

Compared with the conventional complete secondary aluminum plate in Figs. 24–26, the optimized secondary plate structure is reflected in the groove part. By comparing the motor thrust, air gap magnetic density, and back electromotive force of the three different spacing gaps, it can be seen that the electromagnetic thrust changes under the same air gap and the same current excitation condition at the same secondary pole distance. After grooving, the electromagnetic thrust of the motor can be significantly improved by opening the trapezoidal groove of the secondary plate, which can reduce the end effect and increase the thrust to a certain extent. It can be seen from the experimental simulation that the thrust after grooving can be increased to about 200 N–400 N, and from the cost perspective, the cost consumption of the secondary aluminum plate can be reduced to a certain extent by opening a 6 mm slot.

2.5. Derived Secondary Plate Structure

After grooving in the secondary plate, it is found that the electromagnetic thrust can be increased, so it can be considered to insert some high-conductivity materials in the grooving section of the aluminum plate to observe whether the electromagnetic thrust can be further increased.

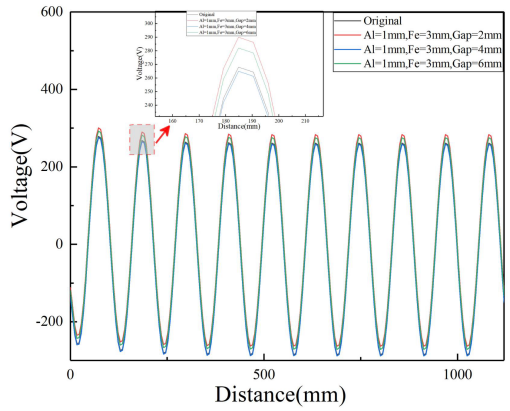

FIGURE 26. Comparison diagram of back electromotive forces of three spacer structures (phase A as an example).

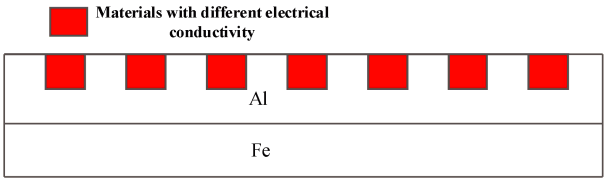

FIGURE 27. Secondary board chimeric topology structure.

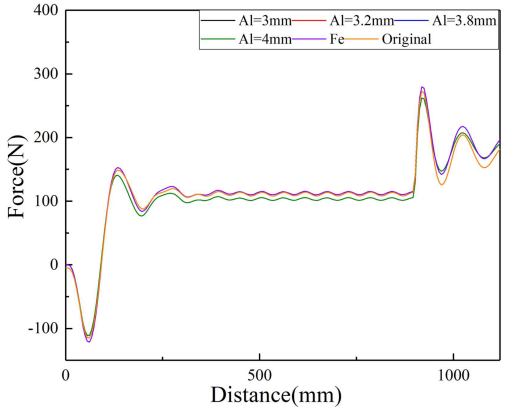

FIGURE 28. Electromagnetic thrust comparison diagram of chimeric structure.

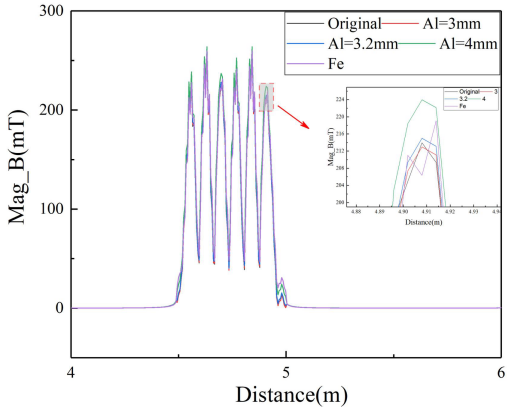

FIGURE 29. Magnetic density comparison diagram of chimeric structure air gap.

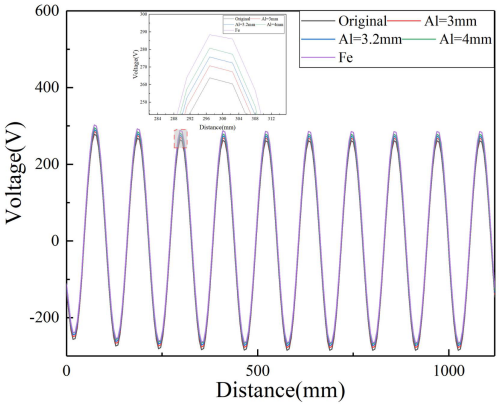

FIGURE 30. Back electromotive force comparison diagram of chimeric structure (phase A as an example).

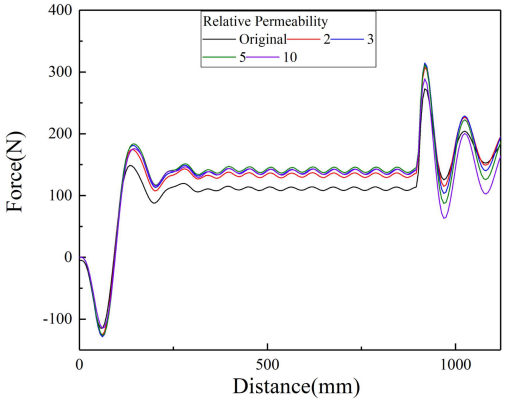

FIGURE 31. Comparison of electromagnetic thrust under different relative permeability.

The specific data of the materials with high conductivity are shown in Table 3.

Through data comparison in in Figs. 27–30, it is found that the aluminum with high or low conductivity in the secondary aluminum plate has no change in the thrust change, but the thrust can be increased in 10–15 N through the Mosaic iron.

2.6. By Increasing the Relative Permeability

Relative permeability for linear induction motors can affect the stator's magnetic field strength, and high permeability materials have a stronger effect on the stator and also help to concentrate the magnetic field to improve the performance and efficiency of the motor. Therefore, from this point of view, different per-

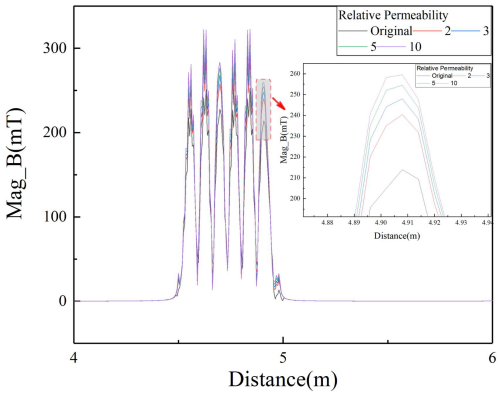

FIGURE 32. Comparison of magnetic density of air gap with different relative permeability.

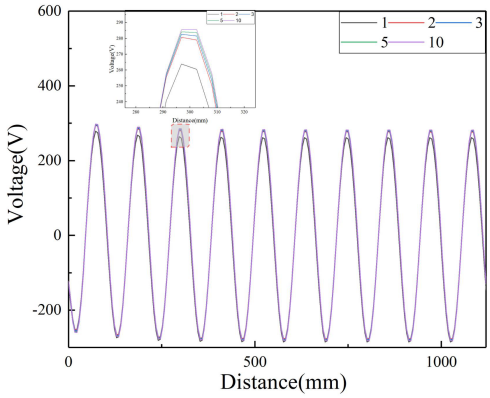

FIGURE 33. Comparison diagram of back electromotive force with different relative permeability (phase A as an example).

TABLE 3. Different conductivity materials.

Initial secondary aluminum plate conductivity	Electrical conductivity of Mosaic structure
$3.8 * 10^7$	$3.0 * 10^7$
$3.8 * 10^7$	$3.2 * 10^7$
$3.8 * 10^7$	$3.8 * 10^7$
$3.8 * 10^7$	$4.0 * 10^7$
$3.8 * 10^7$	$1.03 * 10^7$

meabilities are selected for simulation experiments, and the relative permeability with relatively high thrust is sought.

When the relative permeability is equal to 1, it can be seen that the thrust at this time is the lowest. Since the relative permeability is generally about 1, Maxwell simulation experiments were conducted to test the change of its thrust size by increasing its relative permeability. As shown in the Figs. 31–33, it is found in the experimental data that when the relative permeability was increased, the thrust would increase continuously. However, due to the limitations of practical engineering, the relative permeability cannot reach 10. Therefore, the thrust will increase with the increase of the relative permeability. Therefore, from this perspective, the materials of the secondary plate can be replaced by materials with larger relative permeability to achieve the effect of increasing the motor thrust.

3. CONCLUSION

In this paper, the primary and secondary structures of the short primary single-side linear induction motor are changed to achieve the effect of electromagnetic thrust optimization for the motor. The electromagnetic thrust effects brought by the four structures to the motor are also different:

(1) By adding a chamfer structure at the primary outlet to reduce the eddy current, although the use of chamfer method can increase the electromagnetic thrust, the effect is not obvious, and the corresponding electromagnetic thrust only increases by about 1% to 3%;

(2) By adding a trapezoidal structure of different sizes at the bottom of the primary structure and taking into account the size of the secondary structure of the primary structure, in the final setting when the trapezoidal structure with the bottom edge and height of 0.5 mm is added at this time, the electromagnetic thrust enhancement effect can be improved by about 5%–8%;

(3) The electromagnetic thrust of the motor is optimized by slotting the secondary aluminum plate and inserting materials with different conductivities. Both methods can improve the electromagnetic thrust of the motor and increase the electromagnetic thrust by about 10%;

(4) The secondary plate model of relative permeability is optimized according to the existing permeability, and in an ideal state, it is assumed that a material with high permeability can be manufactured to increase the electromagnetic thrust of the motor to about 30%.

ACKNOWLEDGEMENT

This work was supported in part by National Natural Science Foundation of China under Grant 51807124, Natural Science Foundation of China's Hebei Province under Grant E2021210069 and A2022210024, funded by Science and Technology Project of Hebei Education Department under Grant BJ2020054. Hebei Graduate Student Innovation and Entrepreneurship Funding Project under Grant YC202447.

REFERENCES

[1] Boldea, I., L. N. Tutelea, W. Xu, and M. Pucci, "Linear electric machines, drives, and MAGLEVs: An overview," *IEEE Transactions on Industrial Electronics*, Vol. 65, No. 9, 7504–7515, Sep. 2018.

[2] Lv, G., Z. Zhang, Y. Liu, and T. Zhou, "Characteristics analysis of linear synchronous motor integrated with propulsion, levitation, and guidance in high-speed Maglev system," *IEEE Transactions on Transportation Electrification*, Vol. 7, No. 4, 3185–3193, Dec. 2021.

[3] Boldea, I., *Linear Electric Machines, Drives, and MAGLEVs Handbook*, CRC Press, 2013.

[4] Lv, G., Y. Liu, Z. Zhang, and T. Zhou, "Characteristic analysis of coreless-type linear synchronous motor with the racetrack coils as secondary for EDS maglev train," *IEEE/ASME Transactions on Mechatronics*, Vol. 27, No. 6, 4654–4664, Dec. 2022.

[5] Lv, G., Z. Zhang, Y. Liu, and T. Zhou, "Analysis of forces in linear synchronous motor with propulsion, levitation and guidance for high-speed Maglev," *IEEE Journal of Emerging and Selected Topics in Power Electronics*, Vol. 10, No. 3, 2903–2911, Jun. 2022.

[6] Xia, W., J. Zeng, F. Dou, and Z. Long, "Method of combining theoretical calculation with numerical simulation for analyzing effects of parameters on the Maglev vehicle-bridge system," *IEEE Transactions on Vehicular Technology*, Vol. 70, No. 3, 2250–2257, Mar. 2021.

[7] Sun, Y., J. Xu, G. Lin, W. Ji, and L. Wang, "RBF neural network-based supervisor control for Maglev vehicles on an elastic track with network time delay," *IEEE Transactions on Industrial Informatics*, Vol. 18, No. 1, 509–519, Jan. 2022.

[8] Lv, G., T. Zhou, D. Zeng, and Z. Liu, "Design of ladder-slit secondaries and performance improvement of linear induction motors for urban rail transit," *IEEE Transactions on Industrial Electronics*, Vol. 65, No. 2, 1187–1195, Feb. 2018.

[9] Lu, Q., B. Wu, Y. Yao, Y. Shen, and Q. Jiang, "Analytical model of permanent magnet linear synchronous machines considering end effect and slotting effect," *IEEE Transactions on Energy Conversion*, Vol. 35, No. 1, 139–148, Mar. 2020.

[10] Zhang, Z., M. Luo, J.-A. Duan, and B. Kou, "Performance analysis of double-sided permanent magnet linear synchronous motor with quasi-sinusoidal ring windings," *IEEE Transactions on Energy Conversion*, Vol. 35, No. 3, 1465–1474, Sep. 2020.

[11] Fu, D., Y. Xu, F. Gillon, J. Gong, and N. Bracikowski, "Presentation of a novel transverse-flux permanent magnet linear motor and its magnetic field analysis based on Schwarz-Christoffel mapping method," *IEEE Transactions on Magnetics*, Vol. 54, No. 3, 1–4, Mar. 2018.

[12] Liu, W., H. Yang, and H. Lin, "A hybrid field analytical method of hybrid-magnetic-circuit variable flux memory machine considering magnet hysteresis nonlinearity," *IEEE Transactions on Transportation Electrification*, Vol. 7, No. 4, 2763–2774, Dec. 2021.

[13] Carpita, M., T. Beltrami, C. Besson, and S. Gavin, "Multiphase active way linear motor: Proof-of-concept prototype," *IEEE Transactions on Industrial Electronics*, Vol. 59, No. 5, 2178–2188, May 2012.

[14] Kang, G., J. Kim, and K. Nam, "Parameter estimation scheme for low-speed linear induction motors having different leakage inductances," *IEEE Transactions on Industrial Electronics*, Vol. 50, No. 4, 708–716, Aug. 2003.

[15] Choi, J.-H., S. Kim, D. S. Yoo, and K.-H. Kim, "A diagnostic method of simultaneous open-switch faults in inverter-fed linear induction motor drive for reliability enhancement," *IEEE Transactions on Industrial Electronics*, Vol. 62, No. 7, 4065–4077, Jul. 2015.

[16] Yan, L., L. Zhang, Z. Jiao, H. Hu, C.-Y. Chen, and I.-M. Chen, "Armature reaction field and inductance of coreless moving-coil tubular linear machine," *IEEE Transactions on Industrial Electronics*, Vol. 61, No. 12, 6956–6965, Dec. 2014.

[17] Cao, R., M. Cheng, C. C. Mi, and W. Hua, "Influence of leading design parameters on the force performance of a complementary and modular linear flux-switching permanent-magnet motor," *IEEE Transactions on Industrial Electronics*, Vol. 61, No. 5, 2165–2175, May 2014.